



Discrete element modeling of deformable pinewood chips in cyclic loading test

Yidong Xia ^{a,*}, Zhengshou Lai ^{a,b}, Tyler Westover ^a, Jordan Klinger ^a, Hai Huang ^a, Qiushi Chen ^b

^a Energy and Environment Science & Technology Directorate, Idaho National Laboratory, Idaho Falls, ID, United States

^b Glenn Department of Civil Engineering, Clemson University, Clemson, SC, United States

ARTICLE INFO

Article history:

Received 9 November 2018

Received in revised form 16 December 2018

Accepted 18 December 2018

Available online 22 December 2018

Keywords:

Biomass

Wood chips

Deformable particle

Discrete element method

LIGGGHTS

ABSTRACT

The design of efficient lignocellulosic biomass feedstock systems is challenging, as current laboratory characterization and design methods were developed primarily for fine powders with relatively low compressibility. The discrete element method (DEM) is gaining prominence as an alternative method for modeling the bulk flow and transport of particulate materials in hoppers and feeders. However, prior DEM simulations investigating the flow of wood chips modeled the particles as simple rigid geometries such as spheres, rods or blocks, and neglected the effects of particle deformability and irregular shapes. As a consequence, those simplified DEM models may not provide enough key diagnosis to help improve the design of biomass feeding and handling equipment. This work presents a bonded-sphere DEM approach for characterizing the mechanical behavior of bulk flexible, deformable pinewood chips in a cyclic stress loading test. Clustered spheres that can bend and twist via elastic bonds are used to model irregular-shape particles in real pinewood chip samples. An axial compression tester, which contains 0.06 million bonded-sphere particles (1.35 million spheres) in a quarter cylinder, is simulated with a domain size similar to the experiments. With careful calibration, the simulations have delivered the bulk densities and the bulk moduli of elasticity that are in good agreement with those measured in the corresponding experiments. However, it is also been found challenging for the present DEM model to accurately predict the overall stress-strain behavior of bulk pinewood chips, especially the large sustained plastic deformation during unloading. Additional numerical tests have shown that the adjustment in certain contact parameters (e.g. bond stiffness) can lead to profound solution improvement, but meanwhile will induce extra challenges such as increased computing time. Future work will include an elasto-plastic particle bond model to enhance the simulation fidelity.

© 2018 Elsevier B.V. All rights reserved.

1. Introduction

Loblolly pine forest residues are a low-cost source of biomass for conversion into biofuel or biochemical [1]. Research efforts on instrumented laboratory characterization of bulk mechanical and rheological properties of wood chips have been on the rise recently [2,3], in part because of a growing need for the design of more efficient and durable feedstock systems in biorefinery (e.g. grinder, hopper and feeder). However, a number of limitations have been observed in the current experimental approaches for measuring the required material properties and designing equipment to robustly handle biomass, including residues [4]. In general, the current quantitative methods to design equipment to handle particulate materials were originally devised for powder materials that are relatively incompressible, and that are handled at consolidation pressures larger than about 2 kPa. In many cases, the processes

that handle lignocellulosic biomass for biofuels applications do not meet these criteria, and hence often result in various handling problems [3,5]. For a limited range of applications, the purely empirical methods may be used to successfully design equipment by performing laboratory tests using conditions that are similar to those expected in industrial operations. However, a direct extension of those empirical methods to a wider range of conditions is unlikely practical due to the large number of variables, especially when many of the variables are nonlinearly related. The limitations found in the current experimental and empirical methods indicate that these methods alone do not suffice to satisfy the requirements in biomass characterization. Biomass particles such as processed pinewood chips usually exhibit 1) a wide range of sizes and 2) high complexity of shapes, and are often subject to large deformation and breakage in biomass feedstock refinery and transport processes. Fig. 1 displays representative loblolly pine forest residues that have been hammer-milled with a 25 mm screen. The shapes of individual particles are mostly irregular, with a wide range of sizes from a few millimeters to approximately a centimeter. It is well established that particle shape and size distributions are salient factors that can

* Corresponding author.

E-mail: yidong.xia@inl.gov (Y. Xia).

¹ Approved for external release: INL/JOU-18-51768



Fig. 1. Loblolly pine forest residues after being hammermilled with a 25 mm screen.

significantly affect the bulk behavior of particulate materials [6]. Another factor is that pine chips are relatively soft and can deform considerably even at low stress loading. Predicting the behavior of pinewood chips in feeding and handling processes requires consideration of the above factors to ensure model fidelity.

Originally introduced by Cundall and Strack [7], the discrete element method (DEM) refers to a class of computational models that are widely used for the predictive modeling of the bulk behavior of particulate materials. DEM is similar to molecular dynamics in that it explicitly tracks the motion and often deformation of each particle in the flow field. A review on the major DEM models and applications is reported by Zhu et al. [8]. Moreover, the recent progress in the DEM comminution modeling of mineral ores is summarized in Weerasekara et al. [9], while Horabik and Molenda [10] have reviewed DEM research for agricultural granular materials. Most DEM simulations assume spherical, monodisperse particles because the contact detection and force calculations are simplest and achieve the best scaling in parallel computing. Rackl et al. [11] modeled wood chips as mono-sized spheres in DEM in order to decrease model complexity and reduce simulation time. To compensate the loss of accuracy for using simple spheres, other work adapted the rolling friction parameters of the DEM contact law in spheres to partially mimic the particle shape effects [12]. However, the impact of particle shapes and sizes on the bulk flowability was not further explored. Wood chips have also been modeled with simple non-spherical shapes, such as polyhedron (either ideal or round-edged) and superellipsoids [13–15]. For example, Scherer et al. [16] modeled wood chips as single-body polyhedral particles in a rotary drum. However, their studies did very limited investigation of the impact of particle shape and size on simulation results. To approximate particles with more complex and irregular shapes, two DEM models: the multi-sphere model [17,18] and bonded-sphere model [19] are most often used, as shown in Fig. 2. In the multi-sphere model, many spheres are “glued together” to approximate a rigid, unbreakable particle. Although the model was also applied for

modeling certain kind of wood chips [20], it is apparently not suitable in our case, since it does not consider particle deformability – a factor that significantly affects the bulk flow behavior of pinewood chips (e.g. see Fig. 3). An alternative model, namely the bonded-sphere model, which was initially devised for modeling fracture initiation and evolution across mineral grains in rock [21], can also be used to approximate individual complex-shape particles. In the bonded-sphere model, a particle shape is approximated with a cluster of spheres where each sphere is connected to neighboring spheres with beam like bonds that can be elastically deformed and broken. By adjusting the size and masses of the sphere clusters, the size, shape and mass distributions of pinewood particles can be modeled. The bonded-sphere model is so far the most robust and scalable model in DEM for simulating particulate systems consisting of arbitrarily shaped and deformable particles, despite some known weaknesses when compared with certain specialized models such as the sphero-cylindrical flexible fiber model [22–24] for bendable crop stems [25–28].

Our literature survey, however, has also unveiled a wide scientific gap in the DEM modeling of biomass particulate systems. Most earlier works have focused on the bulk rheological behavior of those particulate materials [6,16,20,29–33], but disregarded the impact of external loading on their bulk mechanical properties (e.g. bulk elasticity) and consequently on their bulk flowability. As of yet, it is unclear what improvements can be made in modeling the mechanical behavior of biomass materials such as wood chips, during hopper flow, auger feeder and grinding operations if particle deformability is considered. Indeed, a quantitative characterization of the bulk mechanical properties of wood particulate materials under external stress loading conditions is a relatively untouched area in DEM modeling. The primary goal of this work is to narrow the aforementioned scientific gap through DEM simulations of bulk wood chips in cyclic compression tests. The particular type of wood chips considered in this work is loblolly pinewood forest residues, as those featured in Fig. 1. Six DEM clustered-sphere particle

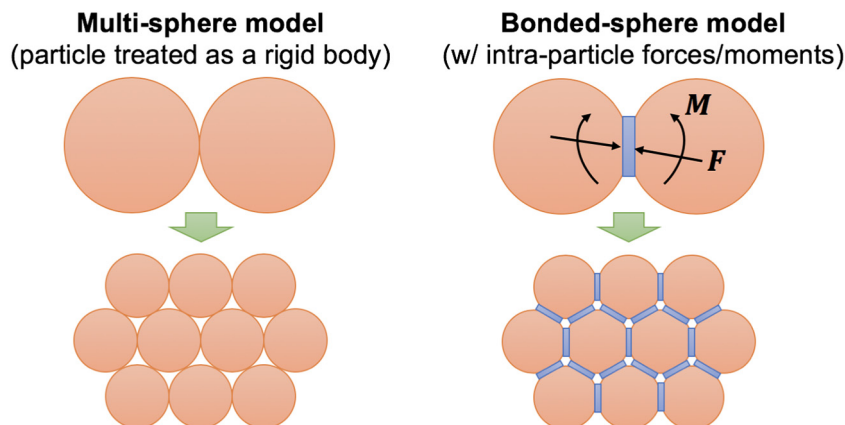


Fig. 2. Illustration of the multi-sphere model (left) and the bonded-sphere model (right).

Mixed fiber- and plate-shape particles: sphere diameter = 1 mm

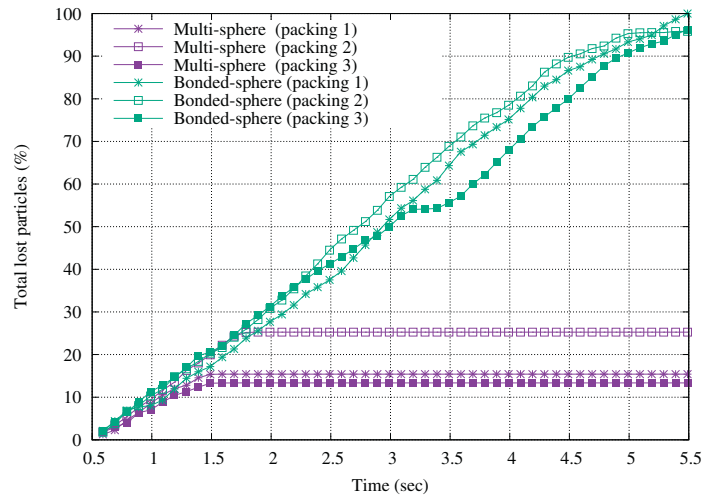
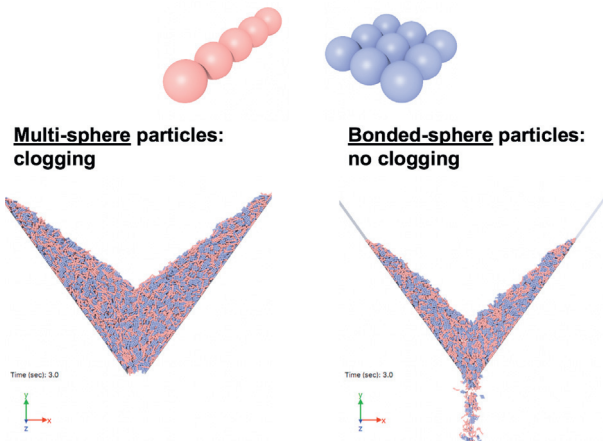


Fig. 3. A hopper simulation test that highlights the impact of particle deformability on particle bulk flowability: the bulk particles consist of a mix of fiber- and plate-shape particles. When using the multi-sphere model, each particle is treated as rigid body, and the hopper is jammed with all three different realizations. However, when using the bonded-sphere model, the particles can deform, and the hopper is able to deplete all particles. Snapshots of simulations on the bottom left correspond to packing 1 at 3 s.

shape templates were created to approximately match the particle size and shape distributions of laboratory samples. To account for particle deformability, the bonded-sphere model is employed to model the individual pinewood particles – a major contribution of this work. Numerical compression tests are performed to assess the bulk mechanical properties of pinewood particles under compression. An equivalent laboratory experiment is conducted in this work as a reference for calibrating the DEM model and validating the simulation results. Since there are very few similar simulations in existing literature, this work presents a new insight into the discussed aspects. The developed workflow and methodology can be easily extended to other woody samples as well as other materials with similar physical features such as miscanthus. Follow-on numerical experiments of hopper flow with the calibrated DEM models are planned in the future.

The rest of the paper is organized as follows. Section 2 briefly describes the formulation of the bonded-sphere DEM model. Section 3 discusses the particle shape conceptualization with the bonded-sphere model. Section 4 presents the detailed setup of the compression test in DEM simulations. Section 5 reports the simulation results, analysis and suggestion for further improvement. Lastly, a summary of this work is provided in Section 6.

2. Bonded-sphereDEM model

The concept of DEM is relatively mature and a general formulation of DEM can be found in Cundall and Strack [7] as well as Chung [34]. In this section, we will present a brief description on the DEM model used in this work. It is not intended to elaborate all aspects of DEM, but rather to provide sufficient background information to present the novel features of the current bonded-sphere DEM model.

2.1. Basic formulation

Within the bonded-sphere DEM model, the motion and deformations of all particles are tracked by calculating the force and moment. The bulk behavior of the material is presented as an assembly of the actions (i.e., the interactions and motion) of all constituent particles. Each particle has two types of motion: translational and rotational, which can be described by the Newton-Euler equations. As to the base

spheres used in this work, the Newton-Euler equations are written as

$$m \frac{d^2 \mathbf{x}}{dt^2} = \mathbf{F} \quad (1)$$

$$I \frac{d^2 \boldsymbol{\theta}}{dt^2} = \mathbf{M} \quad (2)$$

where m and I are the sphere mass and moment of inertia, respectively; \mathbf{x} and $\boldsymbol{\theta}$ are the sphere translational and rotational position; \mathbf{F} and \mathbf{M} are the overall external forces and moments experienced by the spheres; and bold symbols indicate vectors. In order to resolve the motion of each sphere, all the forces/moments experienced by each sphere are first evaluated and summed. A sphere can be subjected to the following typical types of forces/moments: gravity, damping, contact forces, and prescribed external forces. Herein, the damping is particularly referred to the global damping, which is sometimes (artificially) introduced in a DEM model to facilitate energy dissipation and enhance a quasi-static simulation [33,35]. There is another type of damping called local damping, which is usually incorporated into the contact forces accounting for the realistic energy dissipation due to collisions. In this work, only the local damping is considered. For the contact forces, typical contact models would be selected aimed at the particular material of interest. The contact models used in this work for modeling deformable pinewood chips will be presented in a subsequent section. Once the sphere forces/moments are obtained, the sphere motion (i.e., Eq. (2)) is then numerically integrated with a fixed timestep size. For the time integration, a commonly adopted approach is the second order Velocity Verlet algorithm [36]. Consequently, the translational and rotational positions as well as the corresponding velocities of each sphere are updated. The evaluation of sphere forces/moments (especially for the contact forces) and the time integration of sphere motion are resolved cyclically at each timestep through the duration of the DEM simulation.

2.2. Particle representation and contact models

As aforementioned, the irregular-shape pinewood chips are represented by clusters of spheres using the bonded-sphere model (see Fig. 2). The bonded-sphere model was initially devised by Potyondy and Cundall [37] for modeling fracture initiation and evolution across mineral grains in rock. Note that the “bonded-sphere model” was originally referred as “bonded-particle model” in [37]. Here in this work, we will

stick to “bonded-sphere model” since spheres are used as the base elements to form an irregular-shape particle, as well to distinguish the particle within “bonded-particle model” from actual pinewood particles. In bonded-sphere model, the spheres in a same cluster (i.e., particle) are connected with “bonds”, which can be regarded as special contacts that can carry forces and moments. The bonds connect the spheres as a whole, but also allow them to have relative displacements when subjected to external forces/moments. The particle deformation (e.g., bending or deflection) is then replicated from the overall effects of relative displacements of all the spheres within the cluster (i.e., the particle). In this work, the contact forces are calculated from two types of contact models: linear parallel bond model [37] for intra-particle contacts (i.e., the bonds) aiming at capturing the deformation of particles, and Hertz-Mindlin model [38–40] for inter-particle contacts aiming at capturing the collisions between particles. The linear parallel bond model is first proposed by Potyondy and Cundall [37] to analyze rock mechanics. It is simple, but provides constraints to both relative translational and rotational displacements between bonded sphere neighbors. The Hertz-Mindlin contact model is a complete frictional contact model based upon the Hertz theory [38] for contact normal forces and the Mindlin theory Mindlin theory [39] for contact tangential forces. It takes account of the stiffness variation due to the change of contact areas during the collision of two elastic spheres.

3. Characterization of pinewood particles

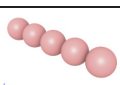
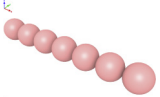
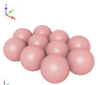
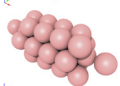
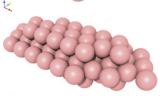
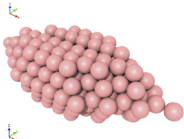
This section presents a numerical conceptualization of real pinewood particles for DEM simulations. In addition, we will also characterize the mechanical behavior of the resulting individual DEM particles to gain insights into the mechanical properties of those particles.

3.1. Particle shape conceptualization

In order to achieve the required fidelity of DEM simulations for predicting the mechanical properties of pinewood particles, the DEM particles need to adequately approximate the shapes and mass distributions of targeted physical materials. Chipped loblolly pinewoods from whole tree debarked chips (*Pinus taeda*) were obtained from TFTX Consulting. The chips were harvested in the fall of 2017 near Brighton,

South Carolina, USA, and were then ground using a Schutte-Buffalo hammer mill (Circ-U-Flow model 18-7-300) equipped with a 25 mm screen. After milling, the sample was sieved using a SWECO Vibro Energy Round Separator (Florence, KY, USA; Model ZS24) equipped with 1 mm and 6 mm sieves to remove large and small particles (i.e. only particles that passed through a 6 mm sieve but did not pass through a 1 mm sieve were used in this study). The sieved samples were divided using rotary or riffle splitters to ensure uniform sample splitting for subsequent tests. Two-dimensional size and shape distributions of the material were obtained using an automated Clemex digital imaging system as described in Hernandez et al. [3]. Though every pinewood particle has a unique shape, most of them can be approximated by some representative shapes such as short stick or thin flake, with maximum length ranging roughly from 5 to 10 mm and maximum width ranging roughly from 1 to 5 mm. This approximation method served as the basis for our particle conceptualization process as follows. In this work, a conceptualization of the sieved pinewood particles resulted in a set of 6 types of irregular-shape DEM particles denoted by A5, A7, B10, B31, C72 and D229, respectively, as listed in Table 1. Each particle type consists of a cluster of base spheres, with all the base spheres having the same diameter of 1 mm. In the particle type notations, the letters are used to categorize the particle cross-section shapes, while the numbers are used to indicate the number of base spheres. Particles in categories A, B, C and D have 1, 3, 5 and 7 rows of base spheres, respectively, as described in Table 1. For example, a B31 particle comprises of 31 base spheres arranged in three rows, and roughly resembles a flake-shape pinewood particle that is 2.7 mm in width, 3.5 mm in length, and 1.0 mm in thickness. The simulated particle size distributions were selected to be approximately the particle width and length distributions of the physical pinewood particles, as shown in Fig. 4. Though we could enhance the particle resolution by using even smaller base spheres (e.g., 0.5 mm in diameter), yet the allowable minimum timestep size for a numerically stable DEM simulation would be reduced by at least 40%, and the total number of spheres would be increased by 5–6 times depending on the packing patterns, resulting in a tremendous increase of computing time by 8–10 times for a same DEM simulation problem. Notice that even with the current particle resolution, over a million base spheres are required to set up a simulation with domain sizes comparable to that in our laboratory

Table 1
Specification of the six DEM particle types in simulations (W/L is short for width/length).

	Type	Layer (spheres)	Row (spheres)	Effective W/L	Mass ratio
	A5	1 (5)	1 (5)	1.0 mm/5.0 mm	7.2%
	A7	1 (7)	1 (7)	1.0 mm/7.0 mm	12.0%
	B10	1 (10)	1 (3), 2 (4), 3 (3)	2.7 mm/3.5 mm	6.5%
	B31	1 (8) 2 (15) 3 (8)	1 (4), 2 (4) 1 (4), 2 (7), 3 (4) 1 (4), 2 (4)	2.7 mm/5.5 mm	15.6%
	C72	1 (17) 2 (38) 3 (17)	1 (5), 2 (7), 3 (5) 1 (6), 2 (8), 3 (10), 4 (8), 5 (6) 1 (5), 2 (7), 3 (5)	3.5 mm/8.0 mm	25.8%
	D229	1 (32) 2 (48) 3 (69) 4 (48) 5 (32)	1 (4), 2 (7), 3 (10), 4 (7), 5 (4) 1 (5), 2 (8), 3 (11), 4 (11), 5 (8), 6 (5) 1 (6), 2 (9), 3 (12), 4 (15), 5 (12), 6 (9), 7 (6) 1 (5), 2 (8), 3 (11), 4 (11), 5 (8), 6 (5) 1 (4), 2 (7), 3 (10), 4 (7), 5 (4)	5.2 mm/13 mm	32.9%

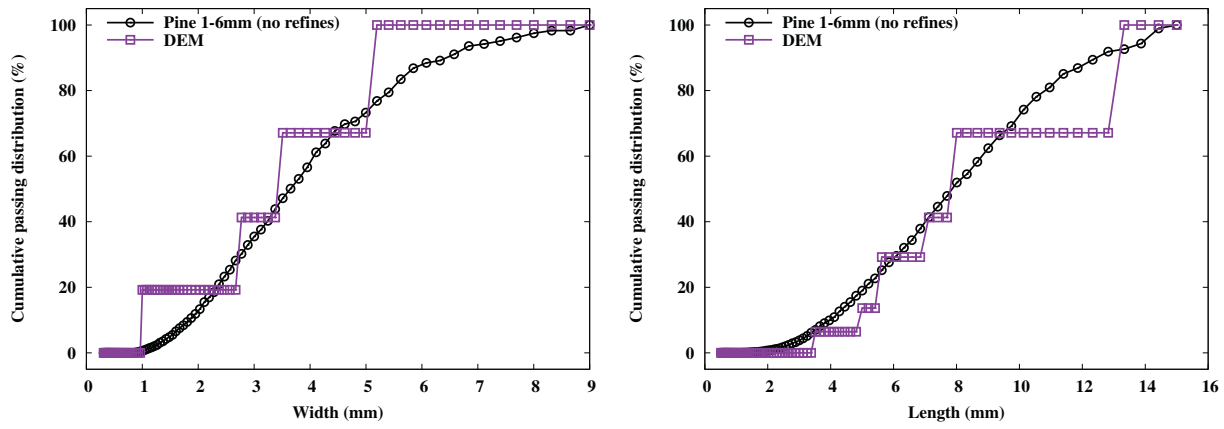


Fig. 4. Approximation of the width and length distributions of the physical pinewood particles (smooth curves) using DEM particles with 6 shapes and thus finite width and length distribution (staircase lines). In this work, we conceptualized the real woodchips into 6 types of DEM shape templates. Each type of DEM template represents real woodchips of a certain range of sizes. As a result, the cumulative distribution of DEM particles is getting steps with each step corresponding to the size of a DEM template.

test. This implies a huge computational costs in our DEM simulations anyhow.

In addition, we conducted a quick validation of the bonded-sphere model by using one A5 particle in a cantilever beam benchmark problem, for which an analytical solution is available for comparison. In this problem, an A5 particle is created with one end sphere fixed, and the other end sphere subject to a constant force perpendicular to the particle length direction. In bond parameter setup, k_n^b is equal to $1 \times 10^{12} \text{ N/m}^3$, while k_s^b is set large enough (i.e., $1 \times 10^{12} \text{ N/m}^3$) to minimize shear displacement between the spheres. The eventual deflection of the particle at equilibrium is recorded and compared to that calculated from the analytical solution. In Fig. 5, the deflection d of the free-end sphere along the direction of the force, agrees well with the analytical solution, which reads $d = FL^3/3EI$, where the circular cross-section area moment of inertia $I = \pi/4(D/2)^4$ with $D = 0.001 \text{ m}$, and for the present problem $L = 0.004 \text{ m}$ and $E = 1 \times 10^9 \text{ Pa}$.

3.2. Correlation between base spheres and clustered particles

A bulk sample of pinewood particles is inherently a multiscale system. To simulate mechanical behavior of such a system, the bonded-sphere DEM model allows us to characterize the system at three length scales successively from bottom to top: 1) the base sphere scale, 2) the clustered particle scale, and 3) the bulk scale. Because the model's mechanical properties of contact (i.e., the Young's modulus, Poisson's ratio, friction coefficient and bond stiffness) are defined based on the sphere-to-sphere interaction, no analytical correlation or formula is readily available to link from one scale to another for a system of

complex-shape particles, e.g. from the sphere scale to particle scale, or from the sphere scale to bulk scale. While the correlation between the sphere scale and bulk scale is to be explored later in Section 5, this section attempts to unveil part of the correlation between the sphere scale and particle scale by using the C72 and D229 particles as examples, as they possess the most complex particle shapes out of the six designed particle types. A bulk of simulated pinewood particles considered in this work contains a large portion of complex-shape particles like C72 and D229. When subject to axial compression, most of the particles in the bulk are unlikely to stay bent like the A5 particle in the cantilever beam bending problem as shown in Fig. 5. Instead, the majority of the complex-shape particles tend to orient with their longitudinal direction of shapes being normal to the direction of the bulk compressive force (or with a tilt of angle larger than 45°). For example, Fig. 6 illustrates our observation in part, where the orientations of the C72 and D229 particles are displayed exclusively out of a mix of the six types of particles under a 2 kPa compressive stress loading. Thus we suggest that a more relevant scenario to investigate is when a complex-shape particle is subject to compressive stress normal to its longitudinal direction of shape.

Now we present a compression test for a C72 particle and a D229 particle, respectively. As displayed in Fig. 7, the two particles contain three and five layers of base spheres, respectively, along the direction of the external force. The spheres in the top layer were applied with compressive forces, while the spheres at the bottom layer were fixed. The compressive force was increased consecutively to provide an equivalent stress (i.e., the compressive force divided by the particle effective cross-section area) from 0.5 to 1, 2 ... and eventually 10 kPa, to mimic

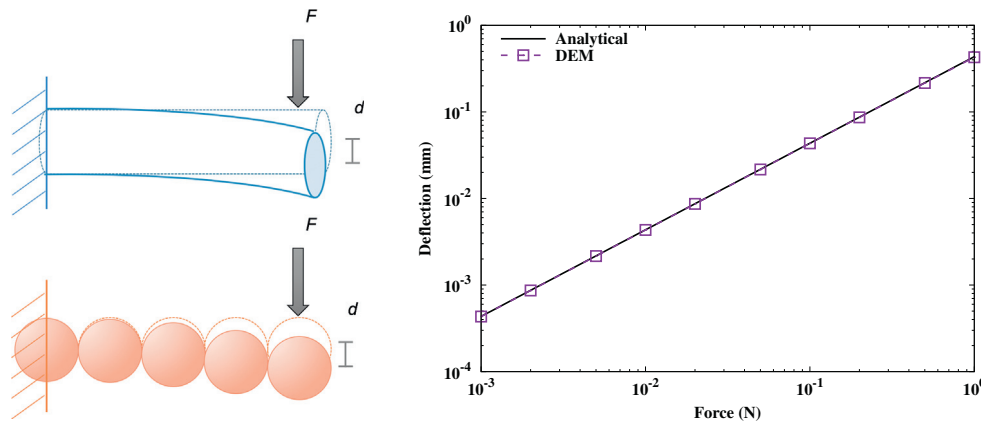


Fig. 5. Validation of the bonded-sphere DEM model with a cantilever beam bending problem.

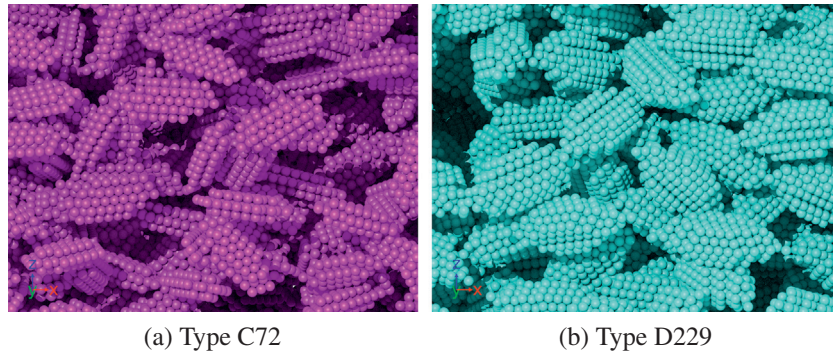


Fig. 6. Orientations of (a) C72 and (b) D229 particles out of the mixed six types of particles under a bulk compression of 2 kPa.

the range of bulk stress in Section 5. For each the compressive stress, the displacements of the spheres in the top layer were recorded and converted to equivalent strains (i.e., the displacements divided by the distance between the loading end and fixed end). Given a range of k_n^b values from 10 to 100 GN/m³ while the sphere Young's modulus $E_s = 0$, the resulting particle Young's modulus E_p values were obtained, as shown in Fig. 7. For each k_n^b tested, E_p is found to be constant, as the compressive strain of the single particles increased almost linearly with the external force. The E_p values are apparently much smaller than the E_s values calculated with an analytical relation for sphere-to-sphere interaction (e.g., $E_s = k_n^b d_s$, where d_s is the sphere diameter). We repeated the compression test with $E_s = k_n^b d_s$ and found that the resulting E_p values are only slightly larger than those with zero E_s , as also shown in Fig. 7. This implies that E_p is relatively insensitive to E_s , and it is important to confirm because the DEM simulation code we employed does not distinguish between the Young's moduli at intra- and inter- particles contacts, which means though we could not set E_s to 0 for intra-particle contacts in bulk compression tests, the simulation results will not be noticeably impacted. Moreover, the calculated E_p values appear a few orders of magnitude smaller than the Young's moduli for tight pinewood blocks in literature. In general, for a real pinewood chip particle, E_p is not geometrically constant, e.g. from surface to interior. Usually, the surface texture of a pinewood chip particle consists of more loose wood fibers and is thus less dense than the inner part of the particle. Though such a test on real pinewood chip particles is not included in this work, we anticipate the E_p to be low at the beginning and higher with the increase of external loading. Following this assumption, we have chosen the E_p values that are much lower in our preliminary DEM simulation test than the Young's modulus for an actual tight pinewood block, which is also a computational strategy to allow the simulations to complete within reasonable time. Therefore, considering all these uncertainties, we recommend that a suitable choice of parameters eventually used in the DEM-based numerical bulk compression test should still rely on bulk scale calibrations.

4. Simulation setup

This section describes the two main steps, 1) initial particle packing, and 2) cyclic stress loading and unloading for setting up DEM simulations of a cyclic axial compression test using a mix of the complex-shape flexible particles devised in the previous section. The simulations are designed based on the corresponding laboratory experiment, which is also conducted as reference for the calibration and validation of the current bonded-sphere DEM model.

4.1. Initial packing

The reference experiment was conducted in a cylindrical container with a radius of 177.8 mm (7 inches). To minimize the computational cost of simulations, we chose to model only a quarter of the container, with the bottom wall in the $z = 0$ plane, a 150 mm-radius cylindrical wall along the z axis, and two virtual symmetry boundaries in the $x = 0$ plane and $y = 0$ plane, respectively. The bottom and cylindrical walls were treated as frictional walls, while the symmetry boundaries were considered as frictionless walls. Notice that the radius of the modeled container is nearly identical to that of the physical tests and is approximately 20 times the mean particle length of 8 mm to minimize the domain size effect in simulations. Table 2 lists the model's contact parameters used in the present simulations, which are a result of limited parameter calibration on certain parameters, e.g. the E and k_n^b . We applied the same set of model parameters to all the base spheres, in order to alleviate the challenge in DEM model parameter calibration.

In our DEM simulations, the initial particle packing is generated with a "rainfall" method, as shown in Fig. 8 (visualized with OVITO [41]). First, packs of particles were inserted periodically from a region above the container and allowed to deposit in the container due to gravity. The insertion region is also a cylindrical volume with a radius of 150 mm and vertical extension from $z = 100$ to 150 mm. The particle insertion was stopped when the height of the bulk sample reached

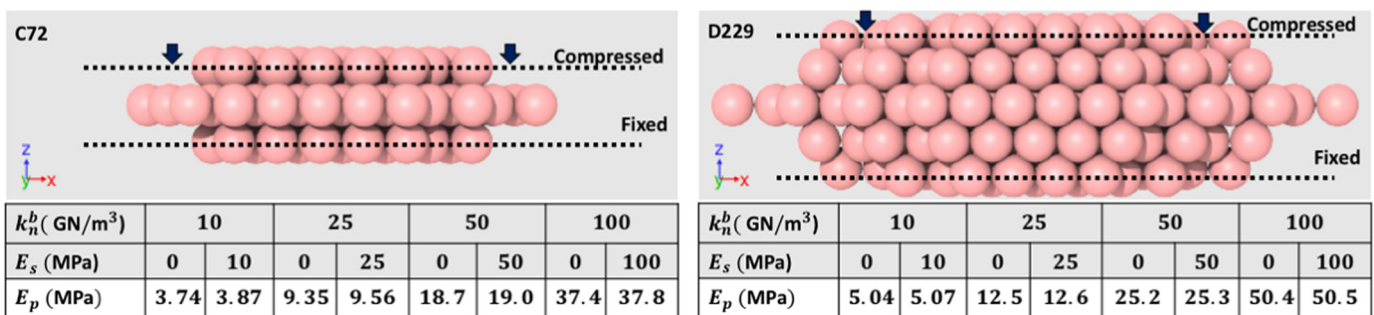


Fig. 7. A uniaxial compression test is conducted to study the relation between the bond normal stiffness (k_n^b) and the resulting particle Young's modulus (E_p) for the C72 and D229 particles, respectively. The sphere Young's modulus (E_s) is set to 0 and $k_n^b d_s$ respectively (where $d_s = 1$ mm) to show that E_p with $E_s = k_n^b d_s$ is only slightly larger than that with $E_s = 0$. E_p is also relatively insensitive to k_n^b . This test suggests that with a specific bonded-sphere particle shape, k_n^b is a leading parameter to determine E_p .

Table 2
Contact parameters of the DEM base spheres used in simulations.

Parameter	Value	Unit
Young's modulus, E	1×10^7	Pa
Poisson's ratio, ν	0.3	–
Coefficient of restitution, e	0.1	–
Particle friction coefficient, μ	0.5	–
Wall friction coefficient, μ_w	0.1	–
Bond normal stiffness, k_n^b	1×10^{10}	N/m ³
Bond shear (tangential) stiffness, k_s^b	6×10^8	N/m ³
Coefficient of bond radius, c_r	1.0	–

well above 100 mm. Then the system was allowed to relax until the mean velocity of the particles became sufficiently small. It is important to note that a large friction coefficient of $\mu = 1.0$ was used until this point, in order to enhance the packing porosity. The simulation was then restarted with $\mu = 0.5$ and allowed to re-equilibrate with time reset from $t = 0$. Due to the sudden reduction of friction, the bulk height of the sample decreased noticeably. Such change also caused a sudden increase of the system kinetic energy, as shown near $t = 0.02$ s in Fig. 9a. Finally, the particles with positions above $z = 100$ mm were removed, which caused another slight increase in the system kinetic energy as seen near $t = 0.32$ s in Fig. 9a. The system was again allowed to relax until the mean velocity of the particles had sufficiently decreased, as displayed in Fig. 9b. The sample obtained in the initial packing contained about 61,900 particles (i.e. 1,348,513 based spheres), corresponding to a porosity of about 60%. Note that when $\mu = 0.5$ was used throughout the whole initial packing process, a lower porosity of 56.4% was obtained. Such comparison suggests that a large μ can be used as a porosity enhancer during particle insertion for creating a loose initial packing. In fact, the bulk porosity measured in physical samples is usually very high, and how to create a high initial packing porosity in DEM simulations is not trivial.

In order to enable quick calibration of the material and contact property parameters, we created a separate simulation setup, denoted as half-size simulation, with the radius and height of bulk sample reduced by half (see Fig. 10), while using the same six types of DEM particles with the same size and mass ratios. The half-size simulation contained about 8,080 particles after initial packing, with the number of the base spheres (164,149) being roughly one-eighth of that in the full-size simulation. A comparison of simulation problem sizes between the full-size and half-size simulations is provided in Table 3. The half-size simulation allows us to identify a suitable set of parameters with a great reduction of computing time. The parameters identified in half-size simulation were then used in the full-size simulation. By doing so,

the domain size effects can be checked as well. The simulation setup described above was selected to mimic the physical experiments in which the pinewood particles were slowly poured into a cylindrical vessel with a diameter of 177.8 mm. The particles were poured to a depth of 100–120 mm, and were then evenly distributed using a flat scraper held at approximately 75° and moved forward to avoid causing compressive stress during the top surface smoothing process.

4.2. Cyclic stress loading and unloading

The initial packing is followed by an axial compression test, as illustrated in Fig. 10. The simulations resembled the main procedures of the laboratory experiment. In the test, six loading & unloading cycles were sequentially operated on the same sample, with peak compressive stresses of 0.5, 1, 2, 3, 4 and 10 kPa, respectively. For example, the 0.5 kPa stress loading was conducted on the sample from the initial packing, and the 1 kPa stress loading was conducted on the same sample after the 0.5 kPa stress was unloaded. At the beginning of the simulation test, a quarter circular surface mesh made of triangular elements was added inside the container with a position slightly above the sample. The mesh is rigid (i.e., deformation ignored) and represents the lid to be pushed downward against the sample to provide the compressive stress. A servo-control mechanism was applied to the lid mesh with a user-specified target stress (e.g. 0.5, 1.0 ... 10 kPa) and user-specified maximum velocity (e.g. 0.1 m/s). The compressive stress being monitored was calculated as an integration of sphere-to-mesh contact forces divided by the area of the quarter lid. During loading & unloading, an automation algorithm was used in the servo-control such that 1) when no particles were detected near the mesh, it moved at the specified maximum velocity; and 2) when particles were detected near the mesh, the lid velocity was reduced to prevent the lid from moving too much within one time step and passing over the neighboring particles. When the calculated stress approached close to the target value, the velocity of the lid was further reduced to allow the stress to reach the target value smoothly. The transient external force and bulk height data were recorded and converted to stress-strain relation for calculating bulk moduli of elasticity.

5. Simulation results

In this section, we report DEM simulation results for the axial compression test with pinewood particles. The simulations were performed with LIGGGHTS [42] (version 4.0.0) on a computing node (36 Intel Xeon E5-2695 v4 CPU cores, 128 GB of RAM, SUSE Linux).

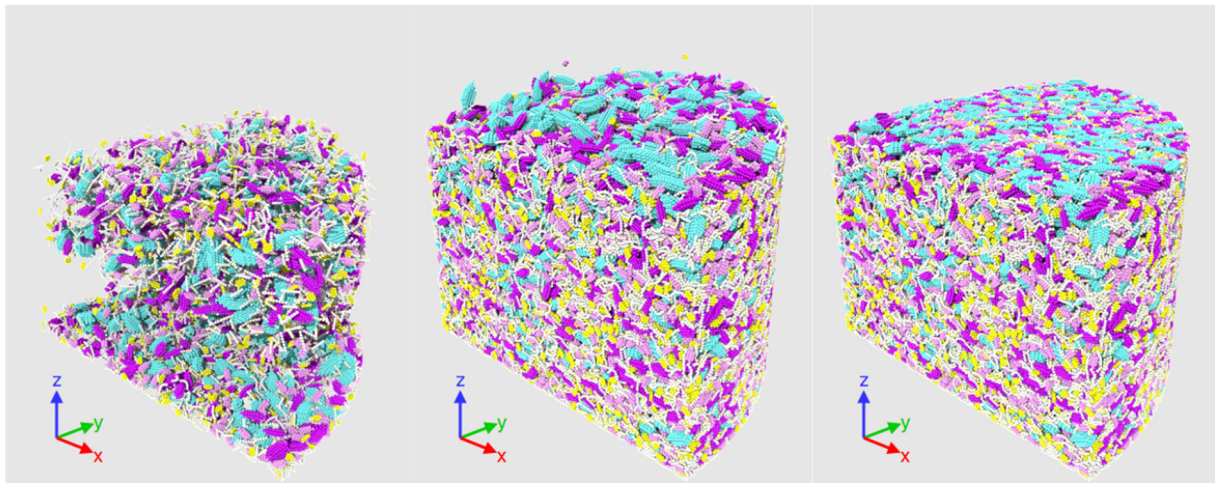


Fig. 8. Initial particle packing with a “rainfall” method. From left to right: insertion by “rainfall”, insertion completed; extra particles removed.

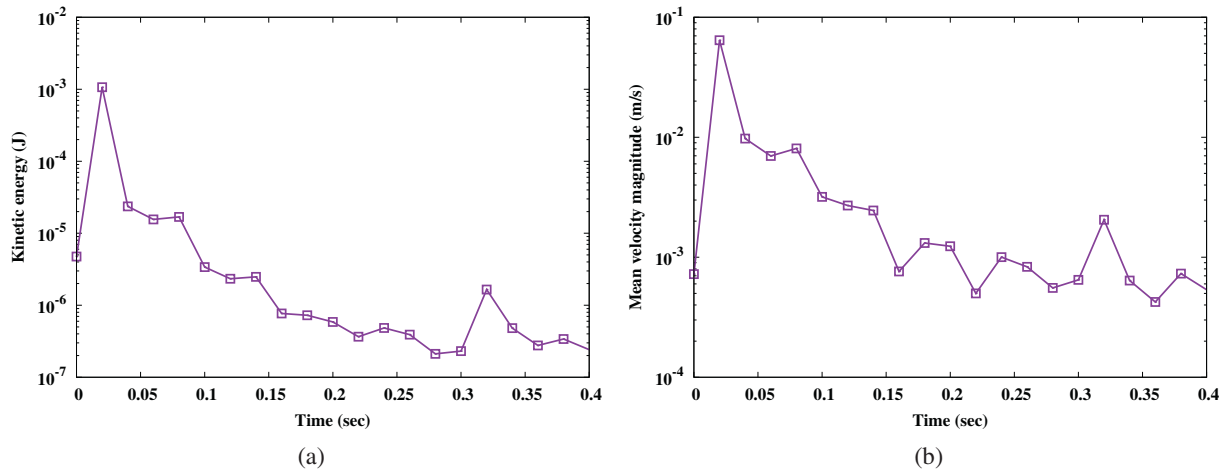


Fig. 9. Time history of (a) the system kinetic energy and (b) the mean velocity magnitude of base spheres since the reduction of friction coefficient from $\mu = 1.0$ to 0.5, until final equilibrium.

The reference physical experiments were performed using an Instron automated load frame (Norwood, MA, USA; model 5967). The maximum speed of the lid varied during the tests but was always regulated to ensure that the instantaneous stress approached the target value smoothly. The target stress values were maintained for 1 min before being relaxed. Four tests were conducted in order to account for possible discrepancies in sample splitting and preparation, although results from only two representative tests are shown here. In DEM simulations of the test, a servo-control mechanism with a higher loading speed (see Subsection 4.2) is adopted to achieve a balance between computational expenses and quasi-static state of simulation. It took 360 hours to simulate a physical time span of 20 seconds (10 million time steps), with a timestep size of $\Delta t = 2$ microsecond (ms) being used. Despite the huge computational cost, simulations are found very helpful for experimentation, as they can unveil more inner details of the test system that the laboratory experiment is not able to measure. For example, Fig. 11 shows the simulated porosity contours of initial packing as well as two typical stress loading states on the lateral cross-section plane at $z = 50$ mm and radial cross-section plane at the 45° angle for $z = 0 - 80$ mm. The porosity distribution in the bulk exhibits strong heterogeneity due to the irregular-shape particles and distributions, but the mean porosity are still around 60% in these planes of initial packing. The simulation results are compared with the

experimental data obtained from the physical tests for validation and calibration. The primary metrics that will be discussed as follows include 1) the bulk stress-strain relations and 2) the bulk density.

5.1. Bulk stress-strain relations

When bulk pinewood chip particles are subject to a sequence of loading & unloading cycles with sequentially increased peak loading stresses, the evolution of the bulk mechanical behavior can be characterized in two phases: Phase 1 for the beginning lower loading & unloading cycles, and Phase 2 for the subsequent higher loading & unloading cycles. During Phase 1 when peak loading stresses are relatively low, the internal structural evolution of the bulk is likely dominated by the irreversible reduction of porosity due to pore collapse and particle reassembling, and as a consequence, the bulk is not expected to fully restore its volume (or height in the present setup) after each unloading. Phase 2 arrives when the peak loading stresses become sufficiently large in the ensuing cycles (but not yet near the threshold to cause particle breakage): the mechanical behavior of the bulk is expected to be more elastic, as the room for the residual porosity to further diminish is much smaller. In the experiments, no breakage of pinewood chips is detected in the samples, which warrants the use of loading stress up to 10 kPa.

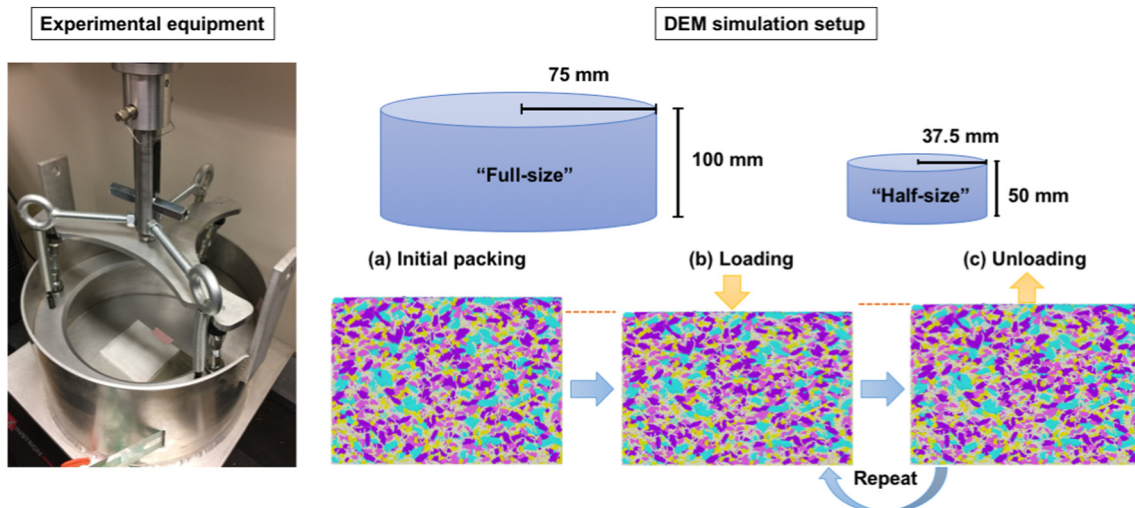


Fig. 10. Illustration of the DEM simulation setup for the cyclic compression test for pinewood chip particles. In the photo image that displays the experimental equipment, the central part of the lid is not installed for showing the interior of the container.

Table 3
Simulation problem sizes.

Metrics	Full-size simulation	Half-size simulation
Diameter of base spheres	1 mm	1 mm
Radius of container	150 mm	75 mm
Bulk height of sample	100 mm	50 mm
Number of particles	about 61,900	about 8,080
Number of base spheres	1,348,513	164,149
Initial packing porosity	60%	61%

Fig. 12 presents a comparison between the simulations and experiments on the full stress-strain histories of the six loading & unloading cycles. The compressive bulk strain ε is calculated by $\varepsilon = (L_0 - L_s)/L_0$, where L_0 is the height of the initial pack (i.e. $L_0 = 100$ mm in the full-size simulation and 50 mm in the half-size simulation), and L_s the transient height of the pack. For clarity, we also plotted each of the cycles individually in Fig. 13, which shows that both the simulations and experiments captured bulk plastic deformation to certain extent in those cycles (e.g. $\Delta\varepsilon = 1\%$ to 3%). A number of main observations are discussed as follows. First, the two experimental curves exhibit a clear difference from the second cycle to the last, in part due to the inherent difference between the two samples. As shown in Fig. 13, the first sample exhibited more plastic deformation than the second one by up to 1.1% throughout the test. Nevertheless, the shapes of the two experimental data curves look similar near all the peak stresses, which indicate consistent bulk mechanical properties between the two samples under compressive stress. Another interesting phenomenon is when the peak stresses were reached and then maintained, the bulk strain continued to increase slightly. For example, as can be seen in Fig. 13f, the two samples underwent a continued bulk deformation by $\Delta\varepsilon = 0.5\%$ when the peak loading stress stayed at 10 kPa. Such creeping phenomenon was not observed in the simulations with the present DEM model, which does not incorporate any rate-dependent contact models.

Regarding the DEM simulation results, the domain size effect is observed between the two simulation curves obtained with the full-size simulation and half-size simulation, as shown in Fig. 12a. A closer comparison in Fig. 13a and Fig. 13b suggests that, though the two simulations have similar initial packing porosity, i.e. 60% versus 61%, more porosity (in terms of percentage) had diminished in the half-size simulation over the first two cycles, which led to about 1% more bulk plastic

deformation. Nevertheless, as seen in Fig. 13c, the two simulations of different sizes behaved quite similarly since the third cycle, despite a pre-existing difference in bulk plastic deformation by 1%. The stress-strain curves obtained with the full-size simulation have a reasonable agreement with their experimental counterparts over the first three cycles, where the simulated curves are bounded by the two experimental data curves (see Fig. 13a–Fig. 13c). In addition, we sampled the stress and strain data in the 89–99% range of each peak stress (e.g. 3.56–3.96 kPa during the 4 kPa loading) for calculating the transient bulk moduli of elasticity, and compared the results between the simulations and experiments in Fig. 14. The values associated to the full-size simulation are consistently lower than their experimental counterparts near each peak stress, but yet bounded in a 20% deviation of the experimental data. The bulk moduli of elasticity in the simulations can be increased with a higher k_n^b value to better match the experimental data. However, a major discrepancy between the simulations and experiments lies in the unloading regions, where the experimental unloading curves are significantly steeper than their simulation counterparts. As a result, the physical samples displayed 1% more bulk plastic deformation than the simulated samples at the end of the test, as shown in Fig. 13f. This contrast suggests that even after the six loadings already conducted, it is highly possible the experimental samples may still contain an abundance of pore spaces that could shrink during subsequent loadings. However, the simulated pinewood particles, which were dominated by bulk elasticity other than plasticity over the last three cycles, exhibited much less plasticity during the unloading processes as well as smaller bulk plastic deformation (i.e. $\Delta\varepsilon \leq 1\%$ as shown in Fig. 13d–f). The small strain recovery during relaxation after the applied stress is removed, even at high stress levels, suggests that plasticity is consistently dominant over elasticity across the entire range of applied stress. The observed changes in the effective Young's modulus and Poisson's ratio (i.e. the slope of the stress-strain curves during relaxation) is likely due to changes in effective particle-particle friction coefficients. This observation indicates that the friction coefficients and other parameters should be considered functions of the strain or void ratio. This behavior is not unexpected because the impact of surface and internal moisture are expected to be strong functions of contact pressure and area, which are dependent upon strain and void ratio. Above all, these findings call for further investigation for enhanced DEM models to account for the large bulk plastic strain in pinewood particles after unloading.

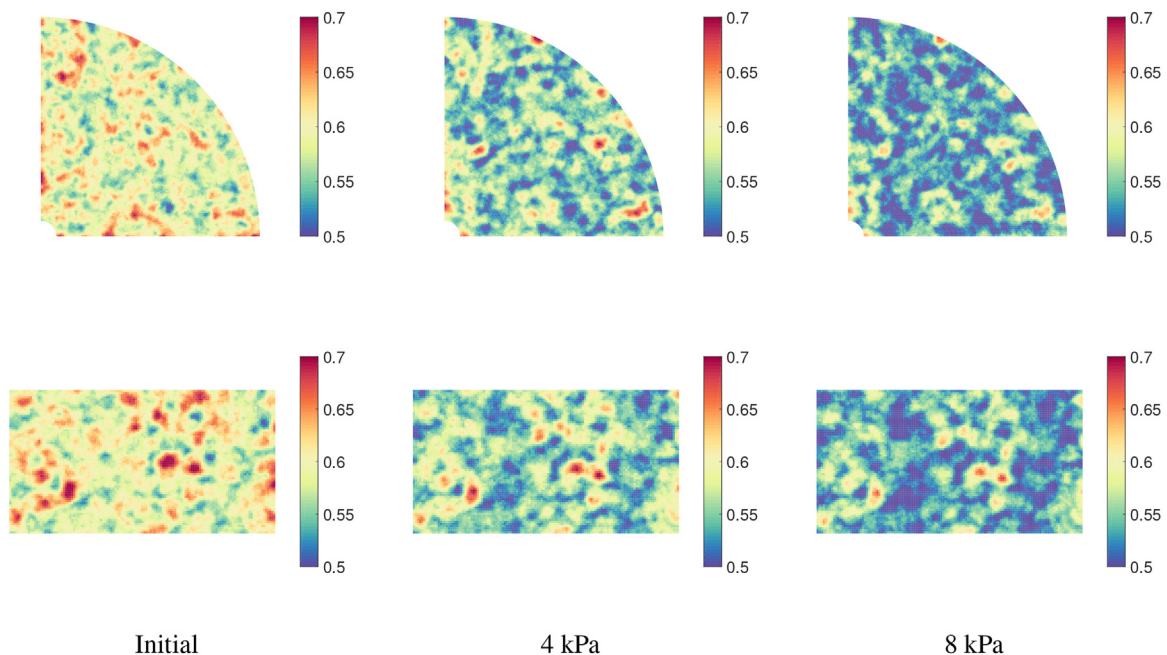


Fig. 11. Porosity contours on horizontal cross-section plane at $z = 50$ mm (top) and vertical cross-section plane at 45° angle (bottom).

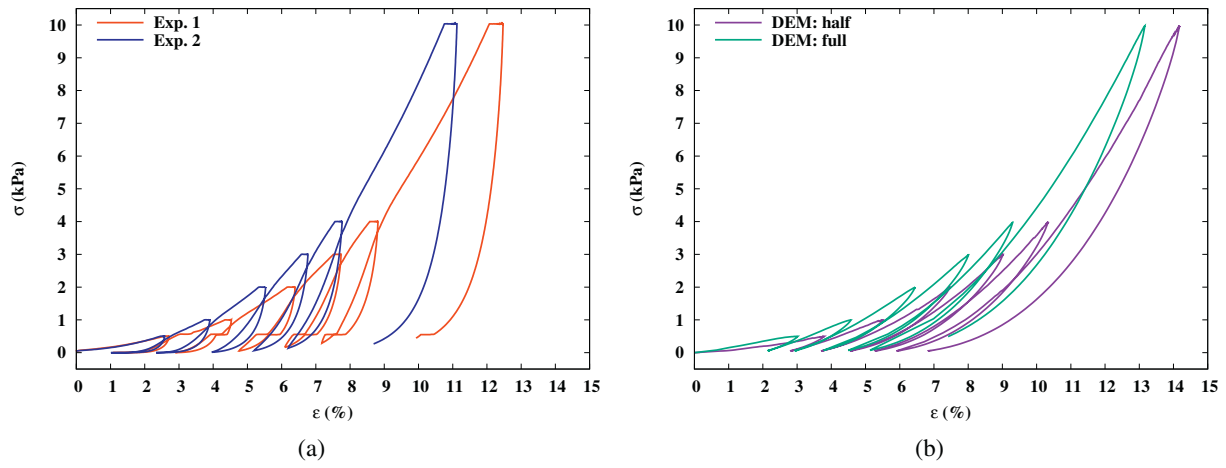


Fig. 12. Comparison of stress-strain curves for the compression test between (a) experiments and (b) simulations.

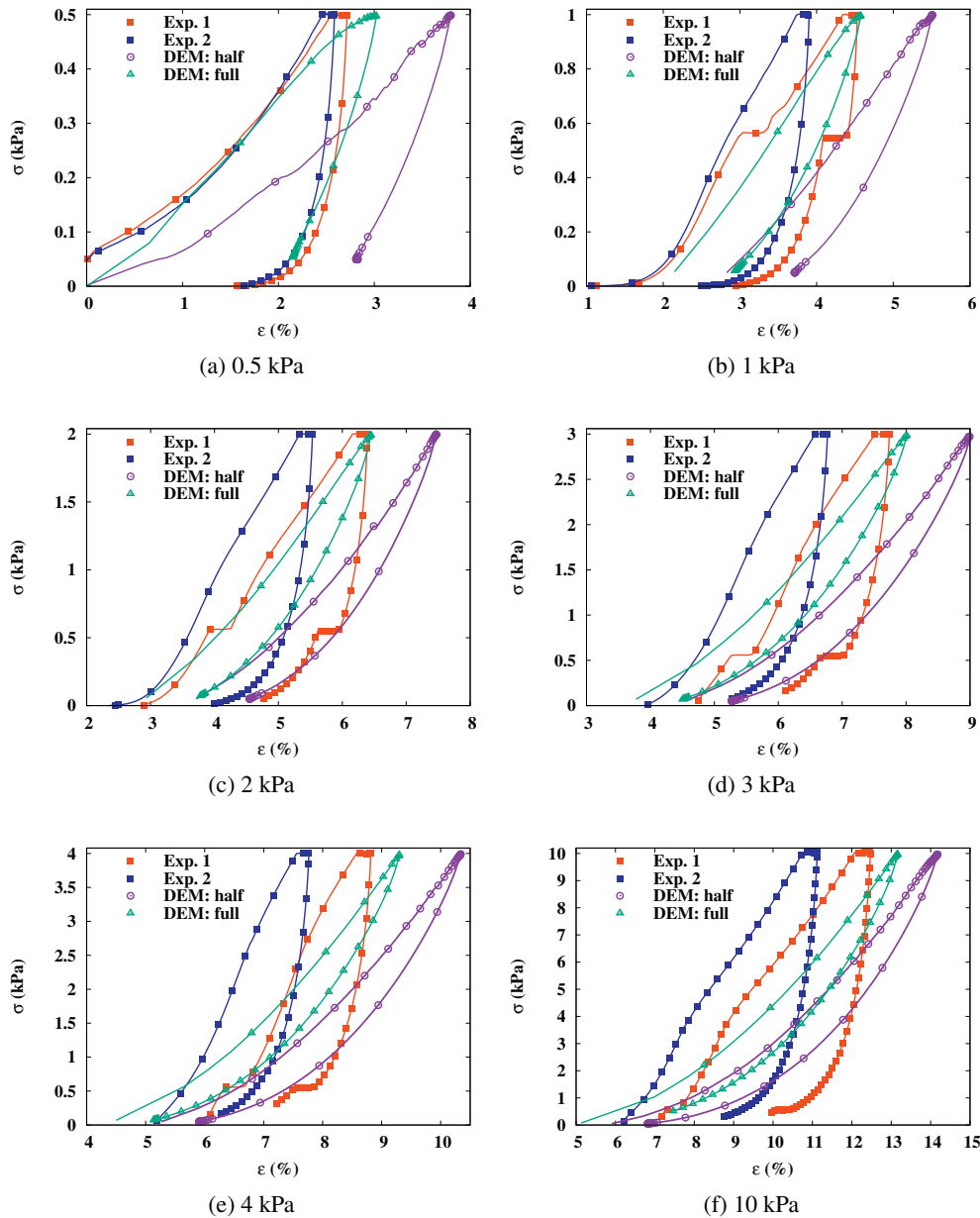


Fig. 13. Comparison of experiment and simulations on the stress-strain histories in individual cycles.

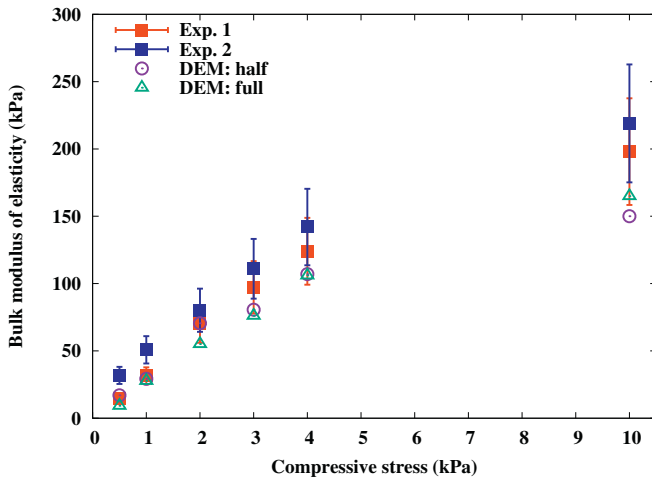


Fig. 14. Comparison between experiment and simulations on the bulk moduli of elasticity near the peak loading stresses. The error bars represent a 20% deviation from the corresponding data.

5.2. Bulk density

Measured at initial packing, the bulk densities of the two physical pinewood chip samples read 169 and 159 kg/m³. The porosities of the physical samples were also measured and used as references for porosity in the DEM simulations. To keep generality in our discussion, we first express the bulk density of particulate materials in the following general form,

$$\rho_{\text{bulk}} = \rho_{\text{grain}} \phi_{\text{grain}} = \rho_{\text{grain}} (1 - \phi_{\text{void}}),$$

where ρ_{grain} denotes the grain density, ϕ_{grain} the grain volume fraction, and ϕ_{void} the bulk porosity, respectively. In bonded-sphere DEM simulations, the ϕ_{void} accounts for the void space between the base spheres only, and can be calculated as

$$\phi_{\text{void}} = 1 - \frac{N_{\text{spheres}} \frac{4}{3} \pi r_{\text{sphere}}^3}{\frac{1}{4} \pi r_{\text{cylinder}}^2 h_{\text{bulk}}}$$

in a quarter cylindrical container, where N_{spheres} is the number of base spheres, r_{cylinder} the container radius, h_{bulk} the bulk height, and r_{sphere} the sphere radius. In the simulations, ϕ_{void} depends on a number of physical constraints such as the particle shapes, particle size distributions and inter-particle friction coefficient. The bound of ϕ_{void} can be roughly estimated if those constraints are specified. For example, with random packing, mono-sized rigid spheres have a statistical lower limit of ϕ_{void} as 36.6%. Recall that our simulated bulk samples have a ϕ_{void} of 60% from initial packing. In contrast, the ϕ_{void} in the physical pinewood particle samples could be higher than the simulations, as the porosity may include not only the macro void between the pinewood particles, but also the micro pore space on the particle surface and inside the particle internal structures.

In order to obtain the ϕ_{void} in the physical samples, we first measured ρ_{grain} with a gas pycnometer, as ϕ_{void} can be calculated from $\phi_{\text{void}} = 1 - \rho_{\text{bulk}}/\rho_{\text{grain}}$. The ρ_{grain} measured is equal to 1398 ± 23 kg/m³, an average of 5 representative splits of the material, with each split measured three times. This value appears much higher than the density of natural pinewood blocks, which range from 400 to 460 kg/m³. Nevertheless, ρ_{grain} values between 1400 and 1600 kg/m³ are often reported for processed wood chips with this technique [43–45]. Based on the measured ρ_{grain} , the calculated ϕ_{void} is equal to 88% and 89% for the physical samples at initial packing, being much higher than their DEM counterpart. Two possible factors are considered

to have contributed to the high ϕ_{void} values (or equivalently ρ_{grain}) in experiments. For the first, the irregular surface structures of realistic pinewood particles at both the macro and micro scales are likely to have created more inter-particle voids than it could be numerically possible in DEM simulations, as the surface of base spheres in our DEM models is assumed smooth. For the second, as mentioned earlier, it is likely that the pore space in our laboratory samples also included internal macro and micro pore structures of the pinewood particles as a result of pressurized open-up and infiltration by the probe gas (e.g. helium). Taking these factors into account, it is legitimate to interpret the relatively low ϕ_{void} in the DEM simulations as the void space external to the particles, and reasonable to use a ρ_{grain} value closer to the density of natural pinewood block for calculating ρ_{bulk} in the DEM simulations.

Fig. 15 displays a comparison of the simulation and experimental results on the bulk density under the six peak compressive stresses in the test. A number of important observations are as follows. First, the two experimental data sets exhibit clear difference in the magnitude of the measured densities (which is common for particulate wood materials in part due to the unavoidable variance between different samples), but much similarity in their increment when the compressive stresses reached higher. For the DEM simulations, the calibrated ρ_{grain} for fitting the experimental data is equal to 410 kg/m³, which is within the density range for natural pinewood block in our case (400–460 kg/m³). We have also found that within this range ϕ_{void} is relatively insensitive to the choice of ρ_{grain} . With the ρ_{grain} value chosen for our model, the curves obtained in both the full-size and half-size simulations are found bounded by the experimental data in a narrow error range of $\pm 10\%$, as shown in Fig. 15, well satisfying our expectation of 80% fidelity for DEM simulations. Moreover, the two simulation curves appear to well agree with each other under all the six peak loading stresses. This indicates that ρ_{bulk} is relatively insensitive to the bulk size in our DEM simulations, as long as the bulk is sufficiently large. Lastly, it is worth noting that the ϕ_{void} is 1% higher in the half-size simulation than that in the full-size simulation at initial packing, which is implied by a smaller initial ρ_{bulk} in Fig. 15. We anticipate this effect is due to the greater impact of wall boundaries in the half-size simulation. When the 0.5 kPa loading was applied, the additional porosity in the half-size simulation diminished quickly and reached the values close to the full-size simulation. This corresponds to the greater bulk plastic strain in the half-size simulation as observed in Fig. 13a.

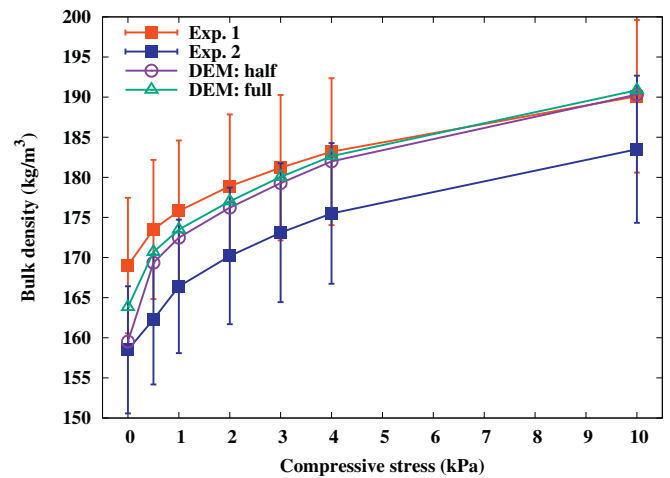


Fig. 15. Comparison between experiment and simulations on the bulk density under the six peak loading stresses. The error bars represent a 10% deviation from the corresponding data.

5.3. Further model calibration

Recall in Section 5.1, the bulk moduli of elasticity near the peak loadings obtained in the simulations are found overall lower than the experiments, as shown in Fig. 14. As suggested earlier, a straightforward way to enlarge the bulk moduli of elasticity in the simulations is to make individual multi-sphere particles less deformable by increasing the bond normal stiffness k_n^b . In addition, we speculate that an increase in k_n^b may also have effect on the bulk mechanical behavior during the stress unloading periods, and subsequently improve our DEM model to better predict the mechanical behavior of bulk pinewood chips. To verify our assumption, we designed two additional simulation tests with the half-size simulation setup, and specified an k_n^b value equal to 10 GN/m³ in the first test and 100 GN/m³ in the second test. These two tests were started from the completed initial packing, but underwent only one stress loading & unloading cycle with a peak stress of 10 kPa, in order to avoid excessive computing time. We did not conduct the full six loading & unloading cycles here, since even a half-size simulation with $k_n^b = 10$ GN/m³ and $\Delta t = 2$ ms requires about 50 h on our 36-core compute node. To make the case even more demanding, the second test which uses $k_n^b = 100$ GN/m³ requires a Δt as small as 1 ms to ensure numerical stability.

The stress-strain relations obtained by the simulation tests are shown in Fig. 16 as green solid curves, and are compared with the experimental curves of the full six cycles. The green solid curve in Fig. 16b appears much more stiff than that in Fig. 16a, confirming a much stiffer bulk elasticity of the particles with a 10 times increase of k_n^b . Meanwhile, the bulk particles in the second test have experienced much less bulk plastic deformation than the first during stress loading, as they are harder and would not deform much to allow the porosity to diminish. During stress unloading, the bulk particles in the second test lost a compressive strain by only 1.5% – much less than the 7% loss of compressive strain in the first test. In order to better compare the two simulation curves with the last cycle in the experimental curve, we shifted them horizontally to allow their peak stress locations to match the experiments, and represented the shifted curves with the green dashed lines. The dashed curve in Fig. 16b indicates a significantly improved simulation result that has a much better agreement with the experimental curve than in Fig. 16a, especially for the stress unloading period. However, as we mentioned earlier, the use of an enlarged k_n^b can not produce large plastic strains during the loading periods (especially at low loading pressures). An enlarged k_n^b also implies a smaller Δt required for numerical stability, which would make these simulations ever more expensive for these tests. A quest for more realistic

elasto-plastic contact models and more cost-effective model calibration methods is anticipated, and deserves more effort in the future.

In the final investigation of this work, we conducted a sensitivity study on the friction coefficient, μ . Following the aforementioned simulation setup for the single-cycle loading & unloading test in which $\mu = 0.5$, we carried out two additional simulations with the μ value doubled, but with all other parameters unchanged. Fig. 17 shows a comparison of the resulting stress-strain relations between the two friction coefficients. The role of friction coefficient is apparently clear: the doubled friction coefficient made the initial porosity in the system harder to demolish with the same external compressive force. As a result, less plastic strain is observed in the case of larger μ . Lastly, we performed a horizontal shift of the lines of $\mu = 1.0$ to make the location of their peak stress tips match those of the lines of $\mu = 0.5$. This allows us to show that even with doubled μ , the stiffness of the system (i.e., the slopes of the lines) did not change much, especially under large stress loading and unloading. To conclude, we have demonstrated that the choice of friction coefficient has noticeable effect on the plastic strain of the system, but meantime much less impact on the stiffness of the system under large stress loading.

6. Summary

A bonded-sphere DEM model based simulation approach has been presented for studying the mechanical behavior of bulk flexible, deformable pinewood chips. Clustered spheres that can bend and twist via elastic bonds have been used to model irregular particle shapes and constituent mass distribution sampled from real bulk pinewood chips. With a careful model calibration, a cyclic stress loading test simulation, which is designed with the size similar to a corresponding laboratory experiment, has been carried out to predict the bulk mechanical behavior of pinewood chips. The bulk densities and compressive moduli of elasticity obtained in the simulations have reached good agreement with the experimental results. However, it has been found challenging for the present DEM model to accurately predict the overall stress-strain behavior of bulk pinewood chips, especially the large sustained plastic deformation during the unloadings. Additional simulation tests have shown that adjustment in certain contact parameters (e.g. bond normal stiffness) could help improve the accuracy of the simulations in terms of some mechanical properties, but meantime would induce additional challenges, such as doubled or even tripled computing time. An elasto-plastic model based on the works of Luding [46,47] will be considered for further enhancing the fidelity of the DEM simulations in the future. Another potential opportunity is to allow values of

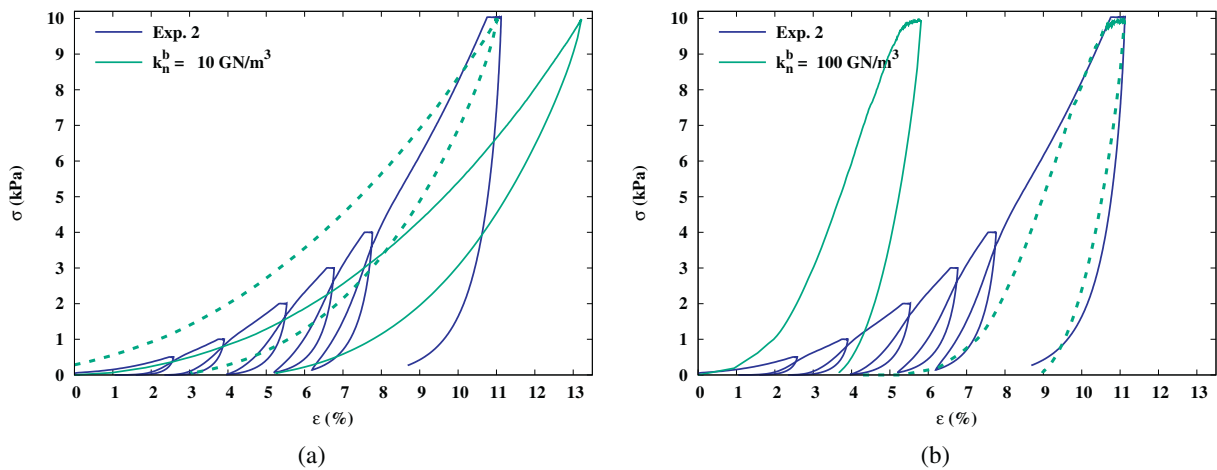


Fig. 16. Stress-strain histories obtained by the two single-cycle loading & unloading simulations with (a) $k_n^b = 10$ GN/m³ and (b) $k_n^b = 100$ GN/m³. The green solid lines are the actual simulation curves; the green dashed lines are a result of horizontal shift to compare the slopes near the 10 kPa peak stress with the physical experiment. (For interpretation of the references to colour in this figure legend, the reader is referred to the web version of this article.)

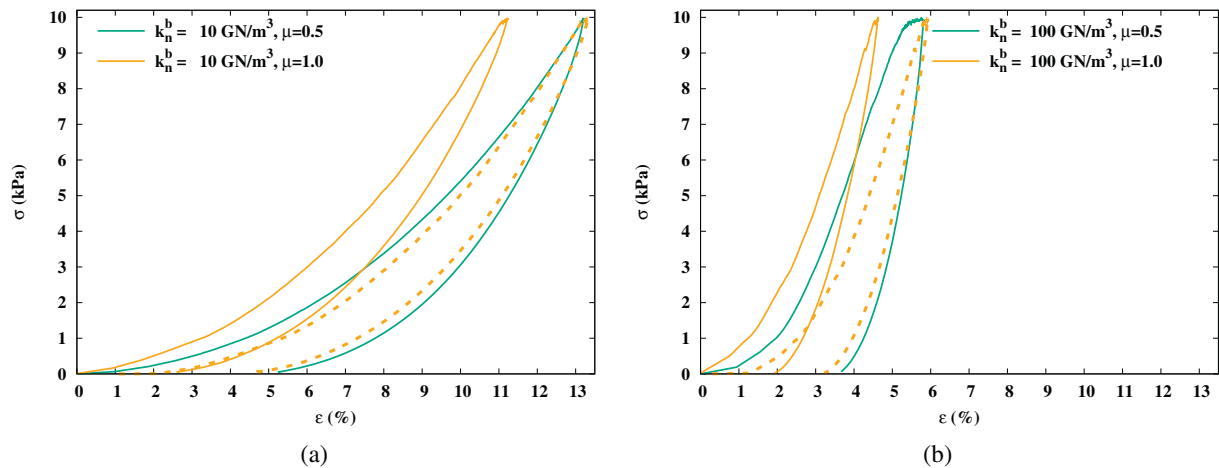


Fig. 17. Stress-strain histories obtained by the single-cycle loading & unloading simulations with (a) $k_n^b = 10 \text{ GN/m}^3$ and (b) $k_n^b = 100 \text{ GN/m}^3$. The green lines correspond to the use of $\mu = 0.5$. The orange solid lines refer to the use of $\mu = 1.0$. The orange dashed lines are a result of horizontal shift of orange solid lines to match the peak stress locations of the green solid lines. (For interpretation of the references to colour in this figure legend, the reader is referred to the web version of this article.)

model parameters, such as particle-particle friction, to depend upon strain or void ratio. Compared with prior DEM works that simulated bulk wood chip flow with simple rigid spheres, rods or blocks, the present work has demonstrated the importance for a DEM model to account for the particle irregular shapes and deformability, in order to better predict the mechanical behavior of bulk wood chips. It is critical to understand that DEM models must reproduce the mechanical behavior of real particulate biomass materials (which are usually relatively soft), in order for the resulting simulations to be of value to provide key diagnosis for helping improve the design of biomass feeding and handling equipment. Above all, a better understanding of the mechanical behavior of the challenging biomass materials will likely require close coupling between instrumented laboratory and pilot scale tests and multi-scale modeling [48].

Acknowledgments

The research is primarily supported by the U.S. Department of Energy (DOE), Office of Energy Efficiency and Renewable Energy (EERE), Bioenergy Technologies Office (BETO), the Feedstock-Conversion Interface Consortium (FCIC), under DOE Idaho Operations Office with Contract No. DE-AC07-05ID14517. This research also receives partial support from BETO with Award Number DE-EE0008255.

References

- [1] U.S. Department of Energy Bioenergy Technologies Office, Strategic Plan for a Thriving and Sustainable Bioeconomy, December 2016.
- [2] M. Stasiak, M. Molenda, M. Bañda, E. Gondek, Mechanical properties of sawdust and woodchips, *Fuel* 159 (2015) 900–908.
- [3] S. Hernandez, T.L. Westover, A.C. Matthews, J.C.B. Ryan, L. Williams, Feeding properties and behavior of hammer-and knife-milled pine, *Powder Technol.* 320 (2017) 191–201.
- [4] T. Westover, D.S. Hartley, Biomass handling and feeding, in: Madhugiri Nageswara-Rao, Jaya R. Soneji (Eds.), *Advances in Biofuels and Bioenergy*, Chapter 6, IntechOpen, Rijeka, 2018.
- [5] D. Barletta, M. Poletto, An assessment on silo design procedures for granular solid biomass, *Chem. Eng. Trans.* 32 (2013) 2209–2214.
- [6] D. Höhner, S. Wirtz, V. Scherer, A numerical study on the influence of particle shape on hopper discharge within the polyhedral and multi-sphere discrete element method, *Powder Technol.* 226 (2012) 16–28.
- [7] P.A. Cundall, O.D.L. Strack, A discrete numerical model for granular assemblies, *Géotechnique* 29 (1) (1979) 47–65.
- [8] H. Zhu, Z. Zhou, R. Yang, A. Yu, Discrete particle simulation of particulate systems: a review of major applications and findings, *Chem. Eng. Sci.* 63 (23) (2008) 5728–5770.
- [9] N.S. Weerasekara, M.S. Powell, P.W. Cleary, L.M. Tavares, M. Evertsson, R.D. Morrison, J. Quist, R.M. Carvalho, The contribution of DEM to the science of comminution, *Powder Technol.* 248 (2013) 3–24.
- [10] J. Horabik, M. Molenda, Parameters and contact models for DEM simulations of agricultural granular materials: a review, *Biosyst. Eng.* 147 (2016) 206–225.
- [11] M. Rackl, F. Top, C.P. Molhoek, D.L. Schott, Feeding system for wood chips: a DEM study to improve equipment performance, *Biomass Bioenergy* 98 (2017) 43–52.
- [12] C.M. Wensrich, A. Katterfeld, Rolling friction as a technique for modelling particle shape in DEM, *Powder Technol.* 217 (2012) 409–417.
- [13] P.W. Cleary, M.L. Sawley, DEM modelling of industrial granular flows: 3D case studies and the effect of particle shape on hopper discharge, *Appl. Math. Model.* 26 (2) (2002) 89–111.
- [14] C.J. Coetzee, Review: calibration of the discrete element method, *Powder Technol.* 310 (2017) 104–142.
- [15] H. Ma, L. Xu, Y. Zhao, CFD-DEM simulation of fluidization of rod-like particles in a fluidized bed, *Powder Technol.* 314 (2017) 355–366.
- [16] V. Scherer, M. Mönnigmann, M.O. Berner, F. Sudbrock, Coupled DEM-CFD simulation of drying wood chips in a rotary drum-baffle design and model reduction, *Fuel* 184 (2016) 896–904.
- [17] M.H. Abbaspour-Fard, Theoretical validation of a multi-sphere, discrete element model suitable for biomaterials handling simulation, *Biosyst. Eng.* 88 (2) (2004) 153–161.
- [18] H. Kruggel-Emden, S. Rickelt, S. Wirtz, V. Scherer, A study on the validity of the multi-sphere discrete element method, *Powder Technol.* 188 (2) (2008) 153–165.
- [19] W. Zhong, A. Yu, X. Liu, Z. Tong, H. Zhang, DEM/CFD-DEM modelling of non-spherical particulate systems: theoretical developments and applications, *Powder Technol.* 302 (2016) 108–152.
- [20] R. Maione, S.K. De Richter, G. Mauviel, G. Wild, DEM investigation of granular flow and binary mixture segregation in a rotating tumbler: Influence of particle shape and internal baffles, *Powder Technol.* 286 (2015) 732–739.
- [21] N. Cho, C.D. Martin, D.C. Sego, A clumped particle model for rock, *Int. J. Rock Mech. Min. Sci.* 44 (7) (2007) 997–1010.
- [22] Y. Guo, C. Wassgren, B. Hancock, W. Ketterhagen, J. Curtis, Validation and time step determination of discrete element modeling of flexible fibers, *Powder Technol.* 249 (2013) 386–395.
- [23] Y. Guo, C. Wassgren, B. Hancock, W. Ketterhagen, J. Curtis, Computational study of granular shear flows of dry flexible fibres using the discrete element method, *J. Fluid Mech.* 775 (2015) 24–52.
- [24] Y. Guo, C. Wassgren, J. Curtis, D. Xu, A bonded spherocylinder model for the discrete element simulation of elasto-plastic fibers, *Chem. Eng. Sci.* 175 (2018) 118–129.
- [25] B. Lenaerts, T. Aertsens, E. Tijssens, B. De Ketelaere, H. Ramon, J. De Baerdemaeker, W. Saeys, Simulation of grain-straw separation by discrete element modeling with bendable straw particles, *Comput. Electron. Agric.* 101 (2014) 24–33.
- [26] P. Langston, A.R. Kennedy, H. Constantin, Discrete element modelling of flexible fibre packing, *Comput. Mater. Sci.* 96 (2015) 108–116.
- [27] T. Leblicq, B. Smeets, S. Vanmaercke, H. Ramon, W. Saeys, A discrete element approach for modelling bendable crop stems, *Comput. Electron. Agric.* 124 (2016) 141–149.
- [28] T. Leblicq, B. Smeets, H. Ramon, W. Saeys, A discrete element approach for modelling the compression of crop stems, *Comput. Electron. Agric.* 123 (2016) 80–88.
- [29] M. Oevermann, S. Gerber, F. Behrendt, Euler-Lagrange/DEM simulation of wood gasification in a bubbling fluidized bed reactor, *Particuology* 7 (4) (2009) 307–316.
- [30] H. Kruggel-Emden, F. Sudbrock, S. Wirtz, V. Scherer, Experimental and numerical investigation of the bulk behavior of wood pellets on a model type grate, *Granul. Mater.* 14 (6) (2012) 681–693.
- [31] D. Höhner, S. Wirtz, V. Scherer, A study on the influence of particle shape on the mechanical interactions of granular media in a hopper using the discrete element method, *Powder Technol.* 278 (2015) 286–305.

- [32] D.L. Schott, R. Tans, I. Dafnomilis, V. Hancock, G. Lodewijks, Assessing a durability test for wood pellets by discrete element simulation, *FME Transactions* 44 (2016) 279–284.
- [33] R. Maione, S.K. De Richter, G. Mauviel, G. Wild, Axial segregation of a binary mixture in a rotating tumbler with non-spherical particles: experiments and DEM model validation, *Powder Technol.* 306 (2017) 120–129.
- [34] Y.C. Chung, Discrete Element Modelling and experimental validation of a granular solid subject to different loading conditions, PhD thesis University of Edinburgh, 2006.
- [35] Itasca Consulting Group, Inc, PFC – Particle Flow Code, Ver. 5.0, Itasca, Minneapolis, 2014.
- [36] L. Verlet, Computer “experiments” on classical fluids. I. Thermodynamical properties of Lennard-Jones molecules, *Phys. Rev.* 159 (1) (1967) 98.
- [37] D.O. Potyondy, P.A. Cundall, A bonded-particle model for rock, *Int. J. Rock Mech. Min. Sci.* 41 (8) (2004) 1329–1364.
- [38] H.R. Hertz, Über die Berührung fester elastischer Körper und Über die Harte, *Verhandlung des Vereins zur Beförderung des Gewerbefleißes*, Berlin, page, 449, , 1882.
- [39] R.D. Mindlin, Elastic spheres in contact under varying oblique forces, *J. Appl. Mech.* 20 (1953) 327–344.
- [40] A. Di Renzo, F.P. Di Maio, An improved integral non-linear model for the contact of particles in distinct element simulations, *Chem. Eng. Sci.* 60 (5) (2005) 1303–1312.
- [41] A. Stukowski, Visualization and analysis of atomistic simulation data with OVITO—the Open Visualization Tool, *Model. Simul. Mater. Sci. Eng.* 18 (1) (2009), 015012.
- [42] C. Kloss, C. Goniva, A. Hager, S. Amberger, S. Pirker, Models, algorithms and validation for opensource DEM and CFD–DEM, *Prog. Comput. Fluid Dyn. Int. J.* 12 (2–3) (2012) 140–152.
- [43] T.E. Redding, K.D. Hannam, S.A. Quideau, K.J. Devito, Particle density of aspen, spruce, and pine forest floors in Alberta, Canada, *Soil Sci. Soc. Am. J.* 69 (5) (2005) 1503–1506.
- [44] G. Hehar, O. Fasina, S. Adhikari, J. Fulton, Ignition and volatilization behavior of dust from loblolly pine wood, *Fuel Process. Technol.* 127 (2014) 117–123.
- [45] G. Olatunde, O. Fasina, S. Adhikari, T.P. McDonald, S.R. Duke, Size measurement method for Loblolly Pine grinds and influence on predictability of fluidization, *Can. Biosyst. Eng.* 58 (2016).
- [46] S. Luding, Anisotropy in cohesive, frictional granular media, *J. Phys. Condens. Matter* 17 (24) (2005) S2623.
- [47] S. Luding, Shear flow modeling of cohesive and frictional fine powder, *Powder Technol.* 158 (1–3) (2005) 45–50.
- [48] T.L. Westover, Y. Xia, J. Klinger, Understanding and solving biomass feeding and handling challenges, *Agric. Res. Technol.* 16 (2) (2018) 001–003.